THE JOURNAL OF PHYSICAL CHEMISTRY C

Article

Cite This: J. Phys. Chem. C 2019, 123, 17644−17649

pubs.acs.org/JPCC

Ignition Threshold of Perovskite-Based Oxides for Solid Fuel Oxidation from First-Principles Calculations

Guangfu Luo,[†] Xizheng Wang,[‡] Michael R. Zachariah,[*,§] and Rohan Mishra[*,†,∥]

[†]Department of Mechanical Engineering and Materials Science and [∥]Institute of Materials Science and Engineering, Washington University in St. Louis, Saint Louis, Missouri 63130, United States

[‡]Department of Chemistry and Biochemistry, University of Maryland, College Park, Maryland 20742, United States

[§]Department of Chemical and Environmental Engineering, University of California, Riverside, California, 92521, United States

Supporting Information

ABSTRACT: Solid oxidants are critical for solid fuel oxidation, such as in chemical looping combustion and solid rocket engines. By combining first-principles calculations, analytic modeling, and experiments on reactions between four types of perovskite-based oxides and aluminum, a prototype solid fuel, we have studied the ignition temperature and reaction kinetics of solid fuel oxidation. We find that oxygen vacancy formation energy serves as a critical parameter in determining the ignition reaction. Specifically, the ignition temperature of each type of structure increases monotonically, but nonlinearly, with the oxygen vacancy formation energy, and the reaction barrier of ignition exhibits structural dependence. Based on our analyses, we predict two materials, $YBa_2Cu_3O_7$ and WO_3, to exhibit low ignition temperature, which is confirmed by subsequent experiments. This study is expected to guide the rational search of new solid oxidants with desirable ignition temperature and ignition kinetics in the vast material space of oxides.

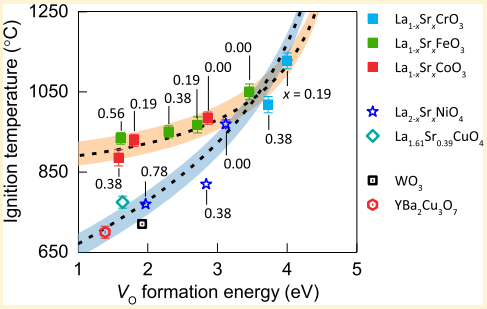

INTRODUCTION

Fuel combustion nominally employs gaseous oxygen because of its easy accessibility in air. There are however technological applications where a gaseous oxygen source is either inaccessible or undesirable. For example, the thermite reaction involves a metallic fuel, commonly aluminum, with a metal oxide as an oxidizer, such as iron oxide.[1] In this case, the metal oxide acts as the oxygen donor and is preferable because an intimate mixture of fuel and oxidant offers more facile reactions than those achievable with the diffusion of gaseous oxygen in a particulate system. In other cases, air is undesirable for environmental concerns. For example, combustion of coal in air under complete combustion conditions leads to a gaseous product stream of CO_2, N_2, and NO_x. However, if CO_2 capture and sequestration is needed,[2] the separation of CO_2 from the gas mixture can be prohibitively expensive.[3] One approach to circumvent this problem is to burn carbon-based fuels with a metal-oxide oxygen donor, which leads to a product stream of nearly 100% CO_2 after water condensation. Such a process is called chemical looping combustion (CLC),[3,4] where the looping refers to the cycling of the metal oxide between the fuel chamber and the air chamber.

The nature of the solid oxidant has been found to profoundly impact the kinetics of solid fuel oxidation. Taking the application in energetic materials as an example, the reaction threshold, commonly referred to as the ignition temperature, varies dramatically by the type of metal oxide but is less dependent on the nature of the fuel (carbon vs aluminum) when the ignition temperature is above the melting point of aluminum.[5] Moreover, the ignition temperature does not linearly correlate with common thermochemical parameters such as heat of reaction or free energy. For CLC, its commercialization also depends heavily on the properties of the oxidant. An ideal oxidant should have a high reaction rate, high oxygen storage capacity, long lifetime, low toxicity, and low cost.[4] Current oxidants usually consist of binary transition-metal oxides, such as Fe_2O_3, NiO, MnO_x, and CuO, but none of them meet all the requirements of an ideal oxidant.[6,7] Promising new solid oxidants can potentially be obtained by going beyond commonly used binary oxides and exploring new binary, ternary, and quaternary oxides, which encompass tens of thousands of compounds.

Therefore, a conceptual understanding that can lead to quantifiable predication of oxidants for solid fuels is desirable. An immediate question that follows is what are the microscopic parameters that control the ignition temperature? Given the multivariate nature of the query, systematic experiments are needed to evaluate the candidate material parameters. In prior work, we employed perovskite oxides for this purpose.[5,8] Perovskite oxides, generally formulated as ABO_3, have been employed in solid oxide fuel cells, solid oxide electrolysis cells,[9] membranes for oxygen separation,[10] and CLC[11,12] because of their high oxygen reactivity, high chemical stability, superior oxygen transport capacities, and flexibility of

Received: February 19, 2019
Revised: June 7, 2019
Published: June 26, 2019

Downloaded via UNIV OF CALIFORNIA RIVERSIDE on December 9, 2020 at 18:42:28 (UTC).
See https://pubs.acs.org/sharingguidelines for options on how to legitimately share published articles.

© 2019 American Chemical Society

DOI: 10.1021/acs.jpcc.9b01609
J. Phys. Chem. C 2019, 123, 17644−17649

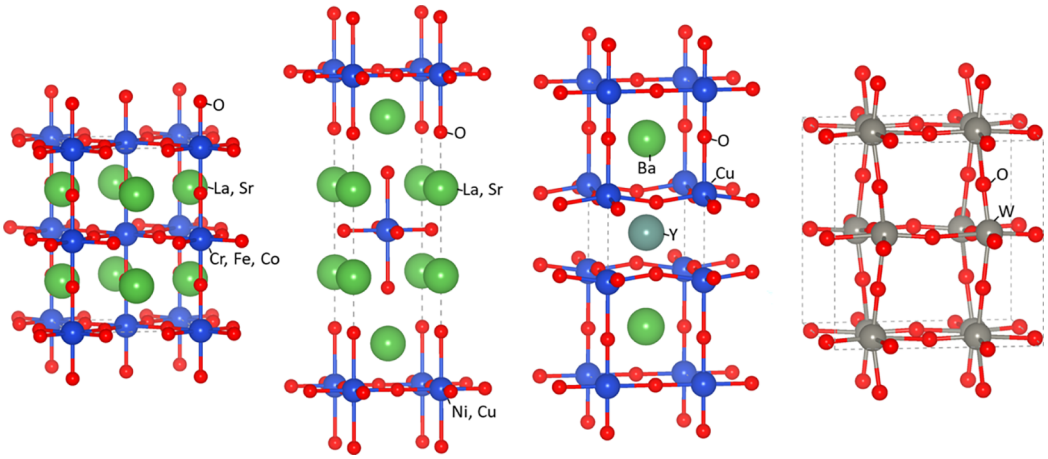

Figure 1. Schematic structures of the four types of transition-metal oxides investigated in this work. First: perovskite oxide, $La_{1-x}Sr_xXO_3$; second: RP oxide with a stoichiometry of $La_{2-x}Sr_xXO_4$; third: $YBa_2Cu_3O_7$; fourth: WO_3.

accommodating a large number of different *A*- and *B*-site cations or partial substitution to adjust the redox properties. In a recent study, Wang et al. found that the ignition of different solid fuels (aluminum, carbon, and tantalum) with doped bismuth oxides or doped perovskites showed systematic trends based on simple bond energy and vacancy concentration analysis.[5,8,13] This suggested an opportunity to develop models that can predict oxidants with ignition temperature for subsequent experiments.

In this work, we have combined first-principles calculations, analytic modeling, and experiments to elucidate the properties of perovskite-based oxides that impact the ignition temperature. We use aluminum nanoparticles as a prototype fuel because the ignition temperature is clearly discernible for their violent reaction, and different oxidizers show similar orders of ignition temperature while using aluminum and carbonaceous fuels as observed in experiments.[5] Interpretation of our experimental results using an ignition-temperature model proposed in this work shows that both ignition temperature and reaction barrier are closely related to the oxygen vacancy (V_O) formation energy: the ignition temperature increases monotonically but nonlinearly with V_O formation energy, and the variation of reaction barrier with V_O formation energy depends on the structure. The results are expected to be valuable for further high-throughput screening of oxidants with desirable ignition kinetics.

Computational and Experimental Details. We have investigated 15 transition-metal oxides that have a perovskite or perovskite-derived structure. These include nine perovskites: $La_{1-x}Sr_xXO_3$ (X = Cr, Fe, and Co; x = 0–0.4), four orthorhombic Ruddlesden–Popper (RP) oxides: $La_{2-x}Sr_xXO_4$ (X = Cu and Ni; x = 0, 0.4), one perovskite-derived orthorhombic structure with layered-ordering of cations and oxygen vacancies: $YBa_2Cu_3O_7$, which has been known as a high-T_c superconductor,[14] and orthorhombic WO_3, a transparent insulator. The schematic structures of these four types of materials are shown in Figure 1. The choice of these materials lies in the fact that they are known to be able to host a significant amount of oxygen vacancies[14−16] and thus expected to have good oxygen transport properties.[17,18]

Our first-principles calculations are based on density-functional theory (DFT) as implemented in the Vienna Ab initio Simulation Package[19] and were carried out with the Perdew–Burke–Ernzerhof exchange–correlation functional.[20] The Hubbard *U* approach is applied to the transition-metal cations with partially occupied d electrons, with an effective *U*–*J* value of 3 eV for Cr, Fe, Co, and Ni, while 5 eV for Cu, according to the FERE approach.[21] To address the metastability issue inherent in the DFT + *U* approach, we adopt the occupation-matrix control method,[22−24] based upon its better performance for locating the ground state than the *U*-ramping[25] and quasi-annealing methods[26] in our tests. The computational procedure for calculating the formation energy of each system using the occupation-matrix control method is as follows. First, we determine all possible diagonal integer occupation matrixes for the primitive cell of a host material (e.g., $LaFeO_3$ is the host material of $La_{1-x}Sr_xFeO_{3-\delta}$) by considering all possible magnetic moments and d-orbital occupations. Second, we fully optimize the primitive cell with each occupation matrix. Third, we lift the occupation matrix and continue relaxing the primitive cell using the wavefunction of the second step as an initial input. Fourth, we use the occupation matrix from the ground state of the primitive cell to optimize a supercell with or without vacancies. The optimization includes changes of both lattice constants and ion positions for supercells without vacancies and only ion positions for those with vacancies. Finally, we lift the occupation matrix and continue relaxing the supercell using the wavefunction of the fourth step as an initial input. Note that symmetry is always turned off to ensure the search of the ground state.[22,24] Following a previous study of oxide perovskites in solid oxide fuel cells, we apply the ferromagnetic state to all systems.[17] Another study has also reported that the ferromagnetic and antiferromagnetic states show similar trends of V_O formation energy for the $LaXO_3$ and $SrXO_3$ (X = Ti, V, Cr, Mn, Fe, Co, Ni, Cu) oxide perovskites.[27] V_O is considered to be neutral in a metallic system but charged with a +2 state in a semiconductor or insulator.

The plane-wave energy cutoff was set to 400–460 eV depending on the systems and the projector augmented-wave method[28] was used, together with the following potentials: La_GW ($5s^25p^65d^16s^2$) for La, Sr_sv_GW ($4s^24p^65s^2$) for Sr, Cr ($3d^54s^1$) for Cr, Fe_GW ($3d^74s^1$) for Fe, Co_GW ($3d^84s^1$) for Co, Ni_GW ($3d^94s^1$) for Ni, Cu_GW ($3d^{10}4s^1$) for Cu, Y_sv_GW ($4s^24p^64d^3$) for Y, Ba_sv_GW ($5s^25p^65d^2$) for Ba, W_sv_GW ($5s^25p^65d^6$) for W, and O_s_GW ($2s^22p^4$) for O. Monkhorst–Pack *k*-point grids were used to sample the

DOI: 10.1021/acs.jpcc.9b01609
J. Phys. Chem. C 2019, 123, 17644−17649

Brillouin zone with a spacing of ~0.28 Å^{-1}. The formation energy of V_O with charge state q is defined by eq 1

$$E_f = E_{tot}(\text{bulk with } V_O) + E_{FNV} + \frac{1}{2}E_{tot}(O_2) - E_{tot}(\text{bulk}) + q[E_{VBM}(\text{bulk}) + E_F] \quad (1)$$

where E_{tot} is the total energy, E_{FNV} contains the ab initio corrections of image charge and potential alignment for a system with defects,[29] E_{VBM} and E_F are the valence band maximum (VBM) of the bulk system without V_O and the Fermi level relative to VBM, respectively. As we are interested in the relative values of V_O formation energy across different materials, we simply use half of the total energy of an oxygen molecule in the triplet state as the chemical potential of oxygen. Given that there are different oxygen sites in these oxides that can have different formation energies, we have used Boltzmann statistics to determine the average formation energy and thereby the overall V_O concentration, using eq 2

$$\overline{E_f} \equiv -k_B T \ln\left(\frac{\sum_i N_i e^{-E_f^i/k_B T}}{\sum_i N_i}\right) \quad (2)$$

where N_i is the number of oxygen sites of type i per supercell and E_f^i is the corresponding formation energy. We set T in eq 2 to 900 °C, given that $\overline{E_f}$ is not sensitive in the entire interval of ignition temperatures of 700 ≤ T ≤ 1200 °C. To examine the impact of thermal lattice expansion, we have also calculated $\overline{E_f}$ of $LaFeO_3$ and $LaCoO_3$ with experiment-based lattices at 900 °C[30,31] and find that the thermal expansion induces changes of less than 0.1 eV in $\overline{E_f}$ (see Section I of Supporting Information).

We obtain the experimental ignition temperature of $La_{1-x}Sr_xXO_3$ (X = Cr, Fe, and Co; x = 0−0.6) from previous experiments[8] and investigate $La_{2-x}Sr_xXO_4$ (X = Cu and Ni; x = 0−0.8), $YBa_2Cu_3O_7$, and WO_3 using similar methods. Specifically, the transition-metal oxides were synthesized by aerosol spray pyrolysis from metal nitrate aqueous solutions formulated with the desired metal ratios. The atomized droplets flowed through a diffusion dryer, where most of the water was absorbed and then passed to a tubular furnace set at 1050 °C to produce the desired perovskite particles. The final product was collected on a Millipore membrane with a pore size of 0.4 μm. Aluminum nanoparticles (~50 nm of diameter) were purchased from Novacentrix Corporation. Stoichiometric mixtures of aluminum nanoparticles and perovskite were physically mixed and sonicated in hexane for 30 min. For control of stoichiometry, a 19% by mass of Al_2O_3 shell was accounted for the aluminum nanoparticles. The hexane suspension of samples was dropped onto a 70 μm-diameter platinum filament, which was heated at a rapid rate of ~4 × 10^5 °C/s to ~1200 °C within 3 ms in the temperature-jump system. Ignition temperature was measured in the temperature-jump/time-of-flight mass spectroscopy (T-jump/TOFMS) using direct optical emission with a high-speed camera (Vision Research Phantom v12.0) operating at 67 056 frames/s. Ignition was determined as the onset of optical emission. More details can be found in ref 8.

RESULTS AND DISCUSSION

Analytic Modeling of Ignition Temperature. The general reaction between a solid oxidant and a fuel can be written as eq 3 because ignition of this class of oxidizers occurs prior to the release of gas phase oxygen.[3,4]

$$\text{Oxidant+fuel} \rightarrow \text{fuel-products+oxidant-with-}V_O \quad (3)$$

According to the Semenov theory of thermal ignition,[32,33] the ignition temperature between an oxidant and a fuel can be defined as the critical temperature at which the heat generation equals the heat dissipation by the surrounding, so any minor increase of heat can accumulate and induce observable phenomena, such as a burst of light or flame. Here, we divide the whole system into two parts: the oxidant−fuel part and the environment. The heat contribution related to the oxidant−fuel reaction (eq 3) equals the reaction rate r times the reaction enthalpy ΔH, that is, $r\Delta H$. Here, we ignore the temperature effects (e.g., lattice vibrations), as they are expected to be similar for the different oxidants considered here with a similar structure. Because we are interested in comparing different oxidants, the fuel and fuel products in eq 3 do not change. Therefore, ΔH is proportional to the V_O formation energy $\overline{E_f}$ (eq 2) together with an energy constant E_0, which equals the reaction enthalpy of O_2 + fuel → fuel-products, as shown in eq 4. When the fuel is aluminum and the fuel product is Al_2O_3 bulk, E_0 equals −5.14 eV according to our DFT calculations.

$$\Delta H \approx \overline{E_f} + E_0 \quad (4)$$

We approximate the reaction rate r of eq 3 with eq 5

$$r = Ae^{-E_a/(k_B T)}[O]^m[\text{fuel}]^n \quad (5)$$

where A is a prefactor, E_a is thereaction barrier related to ignition, [O] and [fuel] denote the concentration of oxygen and reaction sites of fuel at the oxidant/fuel interface, respectively, and m and n are reaction orders and represent the overall process illustrated in Figure 2.

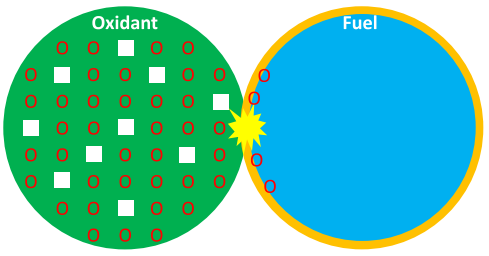

Figure 2. Schematic of ignition reaction between oxidant and fuel. Blank squares in the oxidant represent oxygen vacancies. The outer layer of the fuel is a potential oxide, which is amorphous Al_2O_3 in the case of Al nanoparticles.

For a specific fuel, $[\text{fuel}]^n$ is fixed. If we focus on the same type of oxidant structure, for example, perovskite or RP structure, the concentration of oxygen sites on the surface, [O], can be approximated as a constant. Moreover, similar reaction paths can be expected, as found in reactions occurring on the surfaces of oxide perovskites.[34] Therefore, the Brønsted−Evans−Polanyi principle[35]—namely that the difference in activation barrier between two similar reactions depends linearly on the difference in reaction enthalpy—can

DOI: 10.1021/acs.jpcc.9b01609
J. Phys. Chem. C 2019, 123, 17644−17649

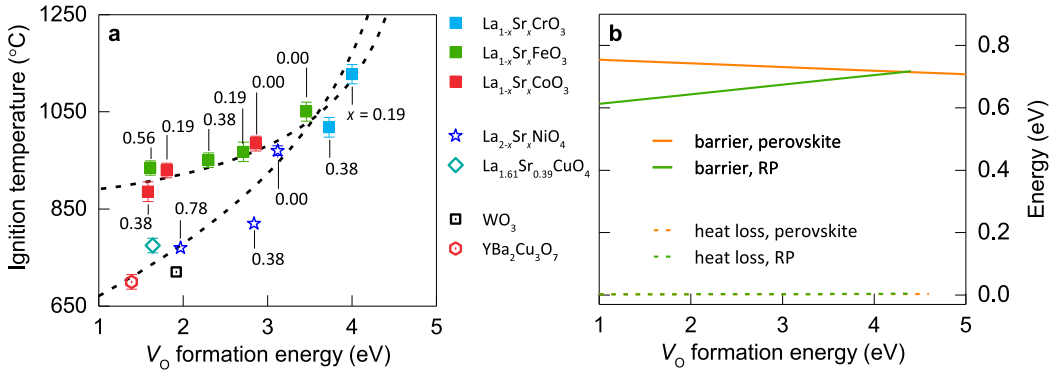

Figure 3. (a) Relationship between experimental ignition temperature and computational V_O formation energy $\overline{E_f}$ for different oxidant−aluminum systems. The dashed fitting curve for perovskite (RP) structures has the parameters of a = −0.0118 (0.0308), c = 0.7662 (0.5818) eV, and γ = 0.03 (0.04). E_0 and $T_{enviroment}$ are −5.14 eV and 300 K, respectively. The shaded regions in (a) indicate the uncertainty interval related to the current data points and model. (b) Reaction barrier, E_a, and heat loss, $\gamma\, k_B(T - T_{enviroment})$, dependence of V_O formation energy $\overline{E_f}$ for perovskite and RP structures.

be used to build a connection between reaction barrier E_a and reaction energy ΔH, as shown in eq 6.

$$E_a \approx a\Delta H + b = a\overline{E_f} + (aE_0 + b) \equiv a\overline{E_f} + c \tag{6}$$

By combining eqs 4−6, we can write the heat generation rate related to eq 3 as eq 7.

$$r\Delta H \approx Ae^{-(a\overline{E_f}+c)/k_BT}[O]^m[\text{fuel}]^n(\overline{E_f} + E_0) = (A[O]^m [\text{fuel}]^n)e^{-(a\overline{E_f}+c)/k_BT}(\overline{E_f} + E_0) \equiv r_0e^{-(a\overline{E_f}+c)/k_BT}(\overline{E_f} + E_0) \tag{7}$$

We define the heat dissipation rate as eq 8, given that both heat conduction and convection depend linearly on the temperature difference between the oxidant−fuel composite and the environment, namely $T - T_{enviroment}$. We have neglected the heat loss through radiation because it is significantly weaker than heat conduction. For instance, for a spherical black body with a diameter of 50 μm and a temperature <1400 K, the radiation power is less than 3×10^{-3} W relative to a 300 K environment temperature; in contrast, the thermal loss through conductance is ∼3 orders higher than the radiation loss assuming an aluminum−oxidant slab with a thickness of ∼50 μm and a thermal conductivity of ∼100 W/(m K), in contact with a 1400 K hot boundary and a 300 K cold boundary. A coefficient r_0k_B is chosen for simplification and γ is a dimensionless parameter related to heat conduction and convection.

$$\text{Heat-loss-rate} \equiv r_0\gamma k_B(T - T_{enviroment}) \tag{8}$$

At the ignition temperature $T_{ignition}$, the sum of energy generation rate (eq 7) and the heat dissipation rate (eq 8) becomes zero, as shown in eq 9.1, which leads to an explicit relation between the vacancy formation energy and the ignition temperature of the oxidant, as shown in eq 9.2.

$$e^{-(a\overline{E_f}+c)/k_BT_{ignition}}(\overline{E_f} + E_0) + \gamma k_B(T_{ignition} - T_{enviroment}) = 0 \tag{9.1}$$

$$\overline{E_f} = -E_0 - k_BT_{ignition}\frac{1}{a}W\left[a\gamma e^{(-aE_0+c)/k_BT_{ignition}}\frac{T_{ignition} - T_{environment}}{T_{ignition}}\right] \tag{9.2}$$

Here W is the product logarithm or Lambert W-function. Note that there is no known explicit expression for $T_{ignition}$. The parameters E_0 and $T_{enviroment}$ can be theoretically calculated or determined in experiments. In our specific case with aluminum as fuel and room-temperature environment, E_0 = −5.14 eV and $T_{enviroment}$ = 300 K. The other parameters, a, c, and γ, can be determined by fitting to the curve of ignition temperature versus V_O formation energy. It is worthy pointing out that the current model assumes that the diffusion process is fast enough to provide all the necessary oxygen to the fuels. When V_O diffusivity becomes low enough, the V_O diffusion kinetics rather than formation energy would determine the ignition temperature. In this context, our examined systems still show a strong correlation between the ignition temperature and V_O formation energy.

Experimental Validation of the Analytic Model. Figure 3a shows the relationship between our calculated V_O formation energy and the experimental ignition temperature for a number of perovskite oxidants reported in a previous article[8] ($La_{1-x}Sr_xCrO_3$, $La_{1-x}Sr_xFeO_3$, and $La_{1-x}Sr_xCoO_3$) and those investigated in this work, including RP structures ($La_{1.61}Sr_{0.39}CuO_4$, $La_{1-x}Sr_xNiO_4$) and two compositions with perovskite-derived structures, $YBa_2Cu_3O_7$ and WO_3, the ignition temperatures of which were first predicted theoretically and subsequently confirmed experimentally. The general trend of V_O formation energy of $La_{1-x}Sr_xCrO_3$, $La_{1-x}Sr_xFeO_3$, and $La_{1-x}Sr_xCoO_3$ is consistent with previous studies,[27,36,37] which however did not investigate several specific compositions examined in this work. Interestingly, a recent study finds that V_O formation energy is also an effective indicator for oxygen release properties of the Mn-containing perovskites.[38] We parameterize eq 9.2 using the data of perovskite and RP structures and find two noticeable trends. First, the ignition temperature increases monotonically but nonlinearly with V_O formation energy for both perovskites and RP structures. Second, the ignition temperature of RP structure is lower than

DOI: 10.1021/acs.jpcc.9b01609
J. Phys. Chem. C 2019, 123, 17644−17649

that of perovskite in the region of $\overline{E_f}$ < 3.5 eV, but the reverse is true when $\overline{E_f}$ > 3.5 eV.

Analysis of the heat loss and reaction barrier in Figure 3b explains the underlying physics of these features. Specifically, the heat loss of all the structures is very similar. However, the reaction barrier of perovskite structures is higher than that of RP structures when $\overline{E_f}$ is low (e.g. 0.75 eV vs 0.61 eV at $\overline{E_f}$ = 1 eV). This difference results in the lower ignition temperature of RP structures than that of perovskites in the region of $\overline{E_f}$ < 3.5 eV. Because the reaction barrier of RP structure increases noticeably while that of the perovskite structures decreases slightly with $\overline{E_f}$, the ignition temperature of RP structure increases faster than that of perovskite structure and finally surpasses it at $\overline{E_f}$ > 3.5 eV.

Finally, we qualitatively discuss the correlation of our fitting parameters with the known properties of perovskite and RP oxides and the predictability of the aforementioned analytic model. One previous experimental study[5] showed that the oxygen ion transport plays a significant role in determining the ignition temperature between solid oxidant and fuel and the oxygen ion mobility is dependent on V_O. In our model, the effect of kinetics is expected to be included in the effective ignition barrier, E_a. Interestingly, our finding that the E_a of perovskite is generally greater than that of RP phases (Figure 3b) is consistent with the fact that the V_O hopping barriers of the former[39,40] are generally greater than those of the latter.[41,42] One prediction of our results on perovskite and RP structures is that lower V_O formation energy generally results in lower ignition temperature. To further verify this trend, we examine two materials with significantly different structures, $YBa_2Cu_3O_7$ and WO_3, and indeed verify this trend, as seen in Figure 3a. Finally, we note that we have also examined the bulk formation energy and find it to be a poor descriptor of the ignition temperature (see Section II of the Supporting Information).

CONCLUSIONS

We have combined first-principles calculations, analytic modeling, and experiments to investigate the ignition temperature and the related reaction kinetics between perovskite-based oxides and aluminum nanoparticles. We find that the V_O formation energy serves as an effective descriptor of the ignition temperature and the reaction kinetics. Our analytic model shows that the ignition temperature increases monotonically but nonlinearly with V_O formation energy, which is verified by our experiments of oxidant with vastly different composition and structures. The framework presented here is expected to be valuable to future high-throughput screening of solid oxidants with optimization of several simultaneous properties, including reaction kinetics, oxygen storage capability, mechanical stability, cost, and toxicity.

ASSOCIATED CONTENT

Supporting Information

The Supporting Information is available free of charge on the ACS Publications website at DOI: 10.1021/acs.jpcc.9b01609.

V_O formation energy in $LaFeO_3$ and $LaCoO_3$ with experimental lattices at 900 °C; relationships between bulk formation energy and V_O formation energy or ignition temperature (PDF)

AUTHOR INFORMATION

Corresponding Authors

*E-mail: mrz@engr.ucr.edu (M.R.Z.).
*E-mail: rmishra@wustl.edu (R.M.).

ORCID

Michael R. Zachariah: 0000-0002-4115-3324
Rohan Mishra: 0000-0003-1261-0087

Notes

The authors declare no competing financial interest.

ACKNOWLEDGMENTS

This work was supported by the Consortium for Clean Coal Utilization at Washington University. R.M. acknowledges support from National Science Foundation grant DMR-1806147. Computations in this work benefited from the use of the Extreme Science and Engineering Discovery Environment (XSEDE), which is supported by National Science Foundation grants ACI-1053575 and ACI-1548562. The authors acknowledge Prof. R. Axelbaum at Washington University for initiating this collaboration. We thank Dr. J. Gazquez of ICMA Barcelona for discussions. M.R.Z. and X.W. acknowledge support from the Army Research Office.

REFERENCES

(1) Wang, L. L.; Munir, Z. A.; Maximov, Y. M. Thermite Reactions - Their Utilization in the Synthesis and Processing of Materials. *J. Mater. Sci.* **1993**, *28*, 3693−3708.

(2) Chu, S. Carbon Capture and Sequestration. *Science* **2009**, *325*, 1599.

(3) Fan, L.-S.; Zeng, L.; Wang, W.; Luo, S. Chemical Looping Processes for CO_2 Capture and Carbonaceous Fuel Conversion−Prospect and Opportunity. *Energy Environ. Sci.* **2012**, *5*, 7254−7280.

(4) Li, J.; Zhang, H.; Gao, Z.; Fu, J.; Ao, W.; Dai, J. CO_2 Capture with Chemical Looping Combustion of Gaseous Fuels: An Overview. *Energy Fuels* **2017**, *31*, 3475−3524.

(5) Wang, X.; Zhou, W.; DeLisio, J. B.; Egan, G. C.; Zachariah, M. R. Doped δ-bismuth Oxides to Investigate Oxygen Ion Transport as a Metric for Condensed Phase Thermite Ignition. *Phys. Chem. Chem. Phys.* **2017**, *19*, 12749−12758.

(6) Yang, W.; Zhao, H.; Wang, K.; Zheng, C. Synergistic Effects of Mixtures of Iron Ores and Copper Ores as Oxygen Carriers in Chemical-Looping Combustion. *Proc. Combust. Inst.* **2015**, *35*, 2811−2818.

(7) Hossain, M. M.; de Lasa, H. I. Chemical-Looping Combustion (CLC) for Inherent CO_2 Separations−A Review. *Chem. Eng. Sci.* **2008**, *63*, 4433−4451.

(8) Wang, X.; Wu, T.; Zachariah, M. R. Doped Perovskites to Evaluate the Relationship between Fuel-Oxidizer Thermite Ignition and Bond Energy, Electronegativity, and Oxygen Vacancy. *J. Phys. Chem. C* **2017**, *121*, 147−152.

(9) Huang, Y.-H.; Dass, R. I.; Xing, Z. L.; Goodenough, J. B. Double Perovskites as Anode Materials for Solid-oxide Fuel Cells. *Science* **2006**, *312*, 254−257.

(10) Schiestel, T.; Kilgus, M.; Peter, S.; Caspary, K.; Wang, H.; Caro, J. Hollow Fiber Perovskite Membranes for Oxygen Separation. *J. Membr. Sci.* **2005**, *258*, 1−4.

(11) Hallberg, P.; Jing, D.; Rydén, M.; Mattisson, A. Chemical Looping Combustion and Chemical Looping with Oxygen Uncoupling Experiments in a Batch Reactor Using Spray-Dried $CaMn_{1-x}M_xO_{3-\delta}$ (M = Ti, Fe, Mg) Particles as Oxygen Carriers. *Energy Fuels* **2013**, *27*, 1473−1481.

(12) Liu, L.; Taylor, D. D.; Rodriguez, E. E.; Zachariah, M. R. Influence of Transition Metal Electronegativity on the Oxygen Storage Capacity of Perovskite Oxides. *Chem. Commun.* **2016**, *52*, 10369−10372.

DOI: 10.1021/acs.jpcc.9b01609
J. Phys. Chem. C 2019, 123, 17644−17649

(13) Wang, X.; Zachariah, M. R. What Atomic Properties of Metal Oxide Control the Reaction Threshold of Solid Elemental Fuels? *Phys. Chem. Chem. Phys.* **2018**, *20*, 26885−26891.
(14) Gazquez, J.; Guzman, R.; Mishra, R.; Bartolomé, E.; Salafranca, J.; Magén, C.; Varela, M.; Coll, M.; Palau, A.; Valvidares, S. M.; Gargiani, P.; Pellegrin, E.; Herrero-Martin, J.; Pennycook, S. J.; Pantelides, S. T.; Puig, T.; Obradors, X. Emerging Diluted Ferromagnetism in High-T_c Superconductors Driven by Point Defect Clusters. *Adv. Sci.* **2016**, *3*, 1500295.
(15) Jang, J. H.; Kim, Y.-M.; He, Q.; Mishra, R.; Qiao, L.; Biegalski, M. D.; Lupini, A. R.; Pantelides, S. T.; Pennycook, S. J.; Kalinin, S. V.; Borisevich, A. Y. In Situ Observation of Oxygen Vacancy Dynamics and Ordering in the Epitaxial $LaCoO_3$ System. *ACS Nano* **2017**, *11*, 6942−6949.
(16) Mishra, R.; Kim, Y.-M.; Salafranca, J.; Kim, S. K.; Chang, S. H.; Bhattacharya, A.; Fong, D. D.; Pennycook, S. J.; Pantelides, S. T.; Borisevich, A. Y. Oxygen-Vacancy-Induced Polar Behavior in $(LaFeO_3)_2/(SrFeO_3)$ Superlattices. *Nano Lett.* **2014**, *14*, 2694−2701.
(17) Lee, Y.-L.; Kleis, J.; Rossmeisl, J.; Morgan, D. Ab initio Energetics of $LaBO_3(001)$ (B = Mn, Fe, Co, and Ni) for Solid Oxide Fuel Cell Cathodes. *Phys. Rev. B: Condens. Matter Mater. Phys.* **2009**, *80*, 224101.
(18) Wachsman, E.; Ishihara, T.; Kilner, J. Low-Temperature Solid-Oxide Fuel Cells. *MRS Bull.* **2014**, *39*, 773−779.
(19) Kresse, G.; Furthmüller, J. Efficient Iterative Schemes for Ab initio Total-Energy Calculations using a Plane-wave Basis Set. *Phys. Rev. B: Condens. Matter Mater. Phys.* **1996**, *54*, 11169−11186.
(20) Perdew, J. P.; Burke, K.; Ernzerhof, M. Generalized Gradient Approximation Made Simple. *Phys. Rev. Lett.* **1996**, *77*, 3865−3868.
(21) Stevanović, V.; Lany, S.; Zhang, X. W.; Zunger, A. Correcting Density Functional Theory for Accurate Predictions of Compound Enthalpies of Formation: Fitted Elemental-Phase Reference Energies. *Phys. Rev. B: Condens. Matter Mater. Phys.* **2012**, *85*, 115104.
(22) Dorado, B.; Amadon, B.; Freyss, M.; Bertolus, M. DFT+U Calculations of the Ground State and Metastable States of Uranium Dioxide. *Phys. Rev. B: Condens. Matter Mater. Phys.* **2009**, *79*, 235125.
(23) Dorado, B.; Amadon, B.; Jomard, G.; Freyss, M.; Bertolus, M. Comment on ″Interplay of Defect Cluster and the Stability of Xenon in Uranium Dioxide from Density Functional Calculations. *Phys. Rev. B: Condens. Matter Mater. Phys.* **2011**, *84*, 096101.
(24) Allen, J. P.; Watson, G. W. Occupation Matrix Control of d- and f-electron Localisations using DFT+*U*. *Phys. Chem. Chem. Phys.* **2014**, *16*, 21016−21031.
(25) Meredig, B.; Thompson, A.; Hansen, H. A.; Wolverton, C.; van de Walle, A. Method for Locating Low-Energy Solutions within DFT +U. *Phys. Rev. B: Condens. Matter Mater. Phys.* **2010**, *82*, 195128.
(26) Geng, H. Y.; Chen, Y.; Kaneta, Y.; Kinoshita, M.; Wu, Q. Interplay of Defect Cluster and the Stability of Xenon in Uranium Dioxide from Density Functional Calculations. *Phys. Rev. B: Condens. Matter Mater. Phys.* **2010**, *82*, 094106.
(27) Curnan, M. T.; Kitchin, J. R. Effects of Concentration, Crystal Structure, Magnetism, and Electronic Structure Method on First-Principles Oxygen Vacancy Formation Energy Trends in Perovskites. *J. Phys. Chem. C* **2014**, *118*, 28776−28790.
(28) Blöchl, P. E. Projector Augmented-Wave Method. *Phys. Rev. B: Condens. Matter Mater. Phys.* **1994**, *50*, 17953.
(29) Freysoldt, C.; Neugebauer, J.; Van de Walle, C. G. Fully ab initio Finite-size Corrections for Charged-defect Supercell Calculations. *Phys. Rev. Lett.* **2009**, *102*, 016402.
(30) Ramaswamy, V.; Awati, P.; Tyagi, A. K. Lattice Thermal Expansion of LaCo1−xCuxO3. *J. Alloys Compd.* **2004**, *364*, 180−185.
(31) Fossdal, A.; Menon, M.; Wærnhus, I.; Wiik, K.; Einarsrud, M.-A.; Grande, T. Crystal Structure and Thermal Expansion of La1-xSrxFeO3-delta Materials. *J. Am. Ceram. Soc.* **2005**, *87*, 1952−1958.
(32) Kim, R.-G.; Jeon, C.-H. Intrinsic Reaction Kinetics of Coal Char Combustion by Direct Measurement of Ignition Temperature. *Appl. Therm. Eng.* **2014**, *63*, 565−576.
(33) Semenov, N. N. *Chemical Kinetics and Chain Reactions*; UK Clarendon Press: Oxford, 1935.
(34) Vojvodic, A.; Calle-Vallejo, F.; Guo, W.; Wang, S.; Toftelund, A.; Studt, F.; Martínez, J. I.; Shen, J.; Man, I. C.; Rossmeisl, J.; Bligaard, T.; Nørskov, J. K.; Abild-Pedersen, F. On the Behavior of Brønsted-Evans-Polanyi Relations for Transition Metal Oxides. *J. Chem. Phys.* **2011**, *134*, 244509.
(35) Brázdová, V.; Bowler, D. R. *Atomistic Computer Simulations: A Practical Guide*; Wiley-VCH: Weinheim, 2013.
(36) Maiti, D.; Hare, B. J.; Daza, Y. A.; Ramos, A. E.; Kuhn, J. N.; Bhethanabotla, V. R. Earth Abundant Perovskite Oxides for Low Temperature CO2 Conversion. *Energy Environ. Sci.* **2018**, *11*, 648−659.
(37) Deml, A. M.; Holder, A. M.; O'Hayre, R. P.; Musgrave, C. B.; Stevanović, V. Intrinsic Material Properties Dictating Oxygen Vacancy Formation Energetics in Metal Oxides. *J. Phys. Chem. Lett.* **2015**, *6*, 1948−1953.
(38) Mishra, A.; Li, T.; Li, F.; Santiso, E. E. Oxygen Vacancy Creation Energy in Mn-Containing Perovskites: An Effective Indicator for Chemical Looping with Oxygen Uncoupling. *Chem. Mater.* **2019**, *31*, 689.
(39) Mastrikov, Y. A.; Merkle, R.; Kotomin, E. A.; Kuklja, M. M.; Maier, J. Formation and Migration of Oxygen Vacancies in La1-xSrxCo1-yFeyO3-delta Perovskites: Insight from ab initio Calculations and Comparison with Ba1-xSrxCo1-yFeyO3-delta. *Phys. Chem. Chem. Phys.* **2013**, *15*, 911−918.
(40) Muñoz-García, A. B.; Ritzmann, A. M.; Pavone, M.; Keith, J. A.; Carter, E. A. Oxygen Transport in Perovskite-Type Solid Oxide Fuel Cell Materials: Insights from Quantum Mechanics. *Acc. Chem. Res.* **2014**, *47*, 3340−3348.
(41) Chroneos, A.; Parfitt, D.; Kilner, J. A.; Grimes, R. W. Anisotropic Oxygen Diffusion in Tetragonal La2NiO4+delta: Molecular Dynamics Calculations. *J. Mater. Chem.* **2010**, *20*, 266−270.
(42) Lee, Y.-L.; Lee, D.; Wang, X. R.; Lee, H. N.; Morgan, D.; Shao-Horn, Y. Kinetics of Oxygen Surface Exchange on Epitaxial Ruddlesden-Popper Phases and Correlations to First-Principles Descriptors. *J. Phys. Chem. Lett.* **2016**, *7*, 244−249.

DOI: 10.1021/acs.jpcc.9b01609
J. Phys. Chem. C 2019, 123, 17644−17649